HOSTED BY

ELSEVIER

Available online at www.sciencedirect.com

ScienceDirect

Journal of Radiation Research and Applied Sciences

journal homepage: http://www.elsevier.com/locate/jrras

Luminescence properties of MgO: Fe^{3+} nanopowders for WLEDs under NUV excitation prepared via propellant combustion route

P.B. Devaraja [a,b,c], D.N. Avadhani [b], H. Nagabhushana [a,**], S.C. Prashantha [d,*], S.C. Sharma [e], B.M. Nagabhushana [f], H.P. Nagaswarupa [d], B. Daruka Prasad [g]

[a] Prof. C.N.R. Rao Centre for Advanced Materials, Tumkur University, Tumkur 572 103, India
[b] Department of Physics, C.M.R.T.U, RV College of Engineering, Bangalore 560 059, India
[c] Department of Physics, Acharya Institute of Graduate Studies, Bangalore 560 090, India
[d] Research Center, Department of Science, East West Institute of Technology, Bangalore 560 091, India
[e] Chattisgarh Swamy Vivekananda Technological University, Bhilai (CG) 493441, India
[f] Department of Chemistry, M.S. Ramaiah Institute of Technology, Bangalore 560 054, India
[g] Department of Physics, B.M.S. Institute of Technology, Yelahanka, Bangalore 560 064, India

ARTICLE INFO

Article history:
Received 27 October 2014
Received in revised form
13 January 2015
Accepted 5 February 2015
Available online 19 February 2015

Keywords:
MgO: Fe^{3+}
Phosphor
Photoluminescence
CCT
CIE Co-ordinates

ABSTRACT

Nanoparticles of Fe^{3+} doped (0–9 mol %) MgO were prepared using low temperature (400 °C) solution combustion technique using glycine as fuel. The powder X-ray diffraction (PXRD) patterns of the as-formed product exhibit cubic phase without further calcination. The effect of Fe^{3+} ions on luminescence properties of MgO was studied and results were discussed in detail. The phosphors exhibit strong red emission upon 378 nm ($^6A_1(^6S) \rightarrow {}^4E(^4G)$) excitation. The characteristic photoluminescence (PL) peaks recorded at ~513, 618 and 720 nm were attributed to transition of $4E + {}^4A_1 ({}^4G) \rightarrow {}^6A_1 ({}^6S)$, $^4T_2 (4G) \rightarrow {}^6A_1$ (6S), $^4T_1 (4G) \rightarrow {}^6A_1$ (6S) respectively. Further, the sample exhibit strong red emission at 720 nm, as a result the phosphor was useful for the applications for (NUV) excitation. The intensity of red emission was attributed to intrinsic defects, especially oxygen-vacancies, which could assist the energy transfer from the MgO host to the Fe^{3+} ions. The Commission International De I-Eclairage chromaticity co-ordinates were calculated from emission spectra and the values (x,y) were very close to National Television System Committee standard value of white emission. Therefore, the present phosphor was highly useful for display applications.

* *Corresponding author*. Tel.: +91 9886021344.
** *Corresponding author*. Tel.: +91 9945954010.
E-mail addresses: bhushanvlc@gmail.com (H. Nagabhushana), scphysics@gmail.com (S.C. Prashantha).
Peer review under responsibility of The Egyptian Society of Radiation Sciences and Applications.
http://dx.doi.org/10.1016/j.jrras.2015.02.001

1. Introduction

In recent years nanometer-sized materials research has increased remarkably due to their unique response to changes in dimensions or shapes within nano scales due to quantum confinement effects (Devaraja, Avadhani, Nagabhushana, et al., 2014; Devaraja, Avadhani, Prashantha, et al., 2014a, 2014b; Naik, Prashantha, Nagabhushana, Nagaswarupa, et al., 2014; Naik, Prashantha, Nagabhushana, Sharma, et al., 2014). Various methods have been reported for the synthesis of oxide nanostructure materials. Among the available chemical methods, solution combustion synthesis (SCS) has been a versatile, simple and rapid process, which allows effective synthesis of wide range of nano-size materials. Depending on the type of the precursors, as well as conditions used for the process, the SCS may occur as either volume or layer-by-layer propagating combustion modes. This process was not only yields nanosized materials but also allows uniform (homogenous) doping of traces of rare-earth impurity ions in a single step (Devaraja, Avadhani, Nagabhushana, et al., 2014; Devaraja, Avadhani, Prashantha, et al., 2014a, 2014b; Fawad, Oh., Park, Kim, & Kim, 2014; Jayalakshmi & Balasubramanian, 2009; Kijima, Yoshinaga, Awaka, & Akimoto, 2011; Nagabhushana et al., 2014; Yang et al., 2014).

Magnesium oxide (MgO), has a wide scientific interest in recent years due to its potential applications in numerous disciplines. MgO has a rocksalt structure with Mg and O atoms octahedrally coordinated, making bulk MgO a diamagnetic material with a wide band gap of 7.8 eV (Tamboli, Patil, Kamat, Puri, & Puri, 2009) and investigated for number of different studies (Moyses Araujo et al., 2010; Sterrer, Fischbach, Risse, & Freund, 2005). Kumar et al. observed that magnetic moments were dependent on the size of nanoparticles that were relevant to the concentration of Mg vacancies (Kumar, Sanyal, & Sundaresan, 2009). Moreover, the nanocrystalline MgO powders, prepared by chemical synthesis, displays ferromagnetic state, attributed to the Mg vacancy defect near the surface of nanograins (Wang, Chen, et al., 2012; Wang, Li, Yang, & Guo, 2012). In contrast to this cation vacancy model, Maoz et al. provided experimental evidence that unpaired electrons trapped at the oxygen vacancy sites may be responsible for the magnetism in a highly defective MgO nanosheet (Maoz, Tirosh, Bar Sadan, & Markovich, 2011). Recently by the density functional calculations have suggested that the substitution of C or N for oxygen in MgO can form impurity pairs, which will interact anti-ferromagnetically with p-type MgO (Yang & Shen, 2005). The transition and rare earth doped MgO host phosphor exhibit wide range of applications as a host for luminescent systems, solid electrolytes, chemical sensors, magnetic refrigeration materials, substrates for high temperature superconductor deposition, catalyst supports and thermal barrier coatings. The broad emission bands can be tunable, making these materials as very attractive by the emission wavelength choice possibility. The doping of inorganic materials with Fe^{3+} at tetrahedral or octahedral sites was also attractive because it allows observable energy transitions in higher and lower energy regions in addition to the broad bands generated in absorption and emission processes (Adamski, Wałesa-Chorab, Kubicki, Hnatejko, & Patroniak, 2014; Orante-Barro et al., 2011; Premkumar et al., 2013; Ren et al., 2009).

In the present work, we report the synthesis and luminescence properties of Fe^{3+} (1–9 mol %) doped MgO nanopowders prepared by low temperature solution combustion method using Glycine as a fuel and its photoluminescence (PL) studies were carried out to predict the luminescence properties of prepared samples.

2. Experimental

2.1. Sample preparation

MgO: Fe^{3+}(0.1–0.9 mol %) nanopowders were prepared by taking stoichiometric quantities of magnesium nitrate ($Mg(NO_3)_2.6H_2O$), ferric nitrate ($Fe(NO_3)_3.9H_2O$) (AR grade, Sigma Aldrich) and glycine [NH_2CH_2COOH] as a fuel using solution combustion method with a procedure discussed elsewhere (Lakshminarasappa, Prashantha, & Singh, 2011). The corresponding nitrates and glycine were dissolved in minimum quantity of double distilled water in a cylindrical Pyrex dish and then mixed uniformly using magnetic stirrer for ~5 min. Thereafter, the Pyrex dish was placed in a preheated muffle furnace maintained at temperature ~400 ± 10 °C. The mixture underwent dehydration and then ignites at one spot with liberation of large amount of gaseous products (nitrogen and carbon) and spreads throughout the reaction mixture. Finally foamy, fluffy and voluminous product was left behind in the Pyrex dish, the final product was crushed into a fine powder using pestle and mortar.

2.2. Characterization

The crystalline nature of the powder samples was characterized by powder X-ray diffraction (PXRD) using Shimadzu X-ray diffractometer (operating at 50 KV and 20 mA by means of Cu-K_α (1.541 Å) radiation with a nickel filter at a scan rate of 2° min^{-1}). The surface morphology of the product was examined by Scanning Electron Microscopy (SEM) Hitachi table top (Model TM 3000). Transmission Electron Microscopy (TEM) analysis was performed on a (JEOL JSM 2100) (accelerating voltage up to 200 kV, LaB_6 filament). Fourier transform infrared spectroscopy (FTIR) studies of the samples were performed with a Perkin Elmer FTIR spectrophotometer. Photoluminescence (PL) studies were made using Horiba, (model fluorolog-3) spectrofluorimeter at RT using 450 W xenon as excitation source and Fluor Essence™ software was used for spectral analysis.

3. Results and discussion

PXRD patterns of undoped and Fe^{3+} doped MgO powder was shown in Fig. 1A. The as-formed samples prepared by solution combustion method show pure single cubic phase without calcination. All the X-ray diffraction peaks of the samples at 2θ, 36.57° (1 1 1), 42.60° (2 0 0), 62° (2 2 0), 74.33° (3 1 1), 78.36° (2 2

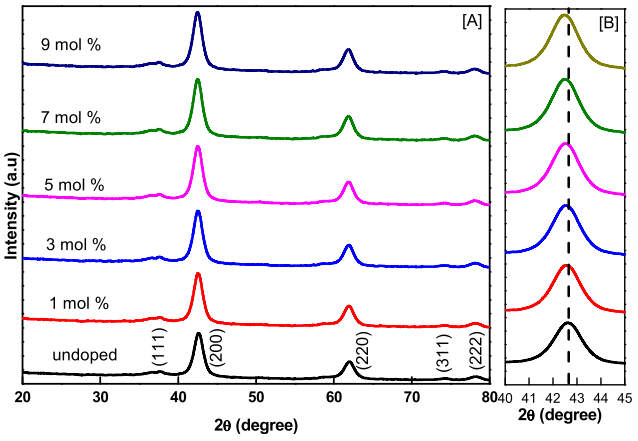

Fig. 1 – PXRD patterns of Fe^{3+} (1–9 mol %) doped MgO nanophosphor.

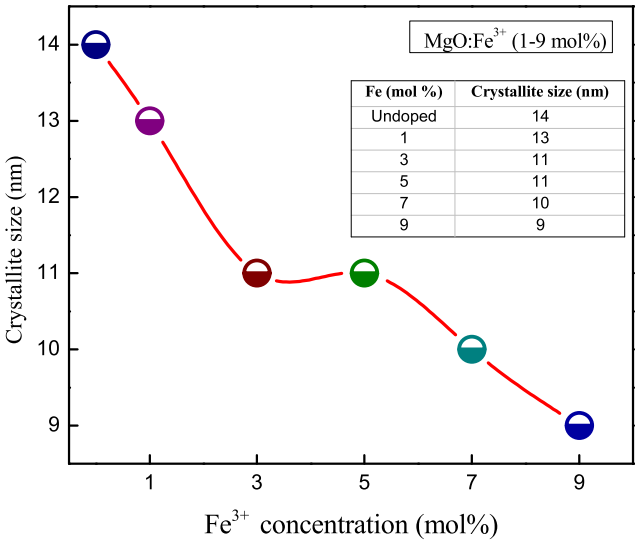

Fig. 2 – Variation of average crystallite size with Fe^{3+} mol % concentration of MgO.

2) were indexed well and matched with JCPDS card No. 4–829 and belong to a space group *fm-3m* (225) (Feng Gu et al., 2008, Devaraja, Avadhani, Nagabhushana, et al., 2014; Devaraja, Avadhani, Prashantha, et al., 2014a, 2014b). For cubic MgO, the average crystallite size (D) was estimated from the line broadening in X-ray powder using Scherrer's formula, lattice parameter and unit cell volume for (2 0 0) plane was estimated using the following the reference

$$D = \frac{0.9\lambda}{\beta \cos\theta} \quad (1)$$

$$2d \sin\theta = n\lambda \quad (2)$$

$$d_{hkl} = \frac{a}{\sqrt{h^2 + k^2 + l^2}} \quad (3)$$

$$V = a^3 \quad (4)$$

where, 'K' constant, 'λ' wavelength of X-rays, and 'β' FWHM. The crystallite size were found to be in the range 5–15 nm, lattice parameter and unit cell volume was found to be 4.3 Å and 79.507×10^{-30} m^3 respectively. It was observed that small amount of Fe^{3+} doping was almost no effect on the MgO crystalline structure, it was direct evident that the introduction of an activator (Fe^{3+}) did not influence the crystal structure of the phosphor matrix. Further, no secondary phase was detected even at 9 mol % doping indicating that Fe^{3+} ions obviously homogeneously mixed and effectively doped in the host lattice in Mg^{2+} sites as the ionic radii was close to each other ($R^{3+}_{Fe} = 0.064$ nm and $R^{2+}_{Mg} = 0.072$ nm).

However, at higher Fe^{3+} doping concentration, the PXRD patterns slightly shifted to lower angle side as shown in the Fig. 1B. Also, it was observed that the crystallite size was found to decreases with increase of Fe^{3+} molar concentration (Fig. 2) indicates that Fe^{3+} ions doped into the host matrix were strongly capped in to the crystal lattice and cause expansion of the unit cell resulting in tensile stress, similar kinds of results were observed in our earlier reports (Prashantha, Lakshminarasappa, & Singh, 2012). Williamson and Hall (W–H) plots (Williamson and Hall., 1953) were used to estimate the micro strain in MgO nanoparticles prepared by combustion method using the relation

$$\beta\cos\theta = \frac{0.9\lambda}{D} + 4\varepsilon\sin\theta \quad (5)$$

where 'ε'; the strain associated with the nanoparticles. The above equation represents a straight line between '4sinθ' (x-axis) and 'βcosθ' (y-axis) (Fig. 3a). The slope of the line gives the strain and intercept of this line on y-axis gives grain size

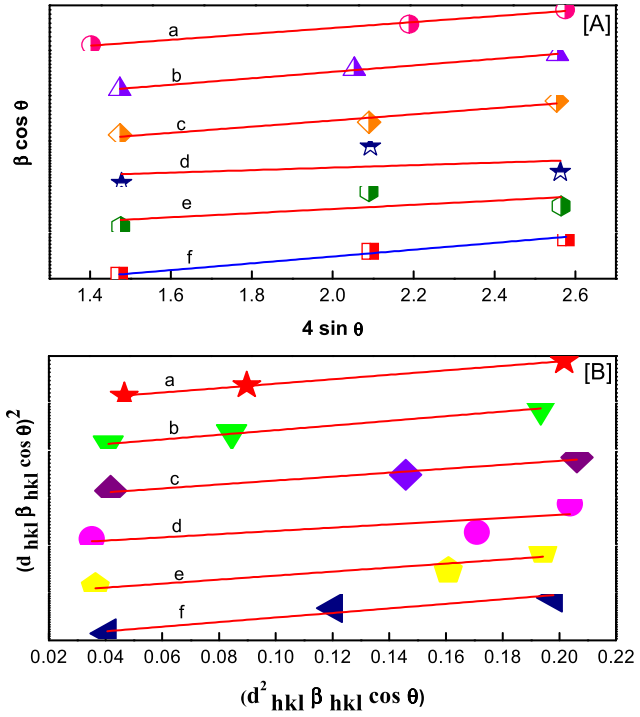

Fig. 3 – (A) W–H plots and (B) Stress–Strain plots of (1–9 mol %) Fe^{3+} doped MgO nanophosphor.

(D). Further, Nelson–Riley method was also used to study size – strain parameters (Fig. 3b). In this method, crystallite size was described by a Lorentzian function and the strain profile by a Gaussian function (Malleshappa et al., 2014). Accordingly, we have

$$(d_{hkl}b_{hkl}\cos\theta)^2 = \frac{k\lambda}{D}\left(d_{hkl}^2 b_{hkl}\cos\theta\right) + \left(\frac{\in}{2}\right)^2 \quad (6)$$

where k; constant that depends on the shape of the particles; for spherical particles it was given as ~ 0.9. Similarly to the W–H plots, the term (d_{hkl} β_{hkl} cos θ) was plotted with respect to (d^2_{hkl} β_{hkl} cos θ) for all the orientation peaks of MgO. In this case, the crystallite size was determined from the slope of the linearly fitted data and the root of the intercept gives the strain.

To get exact lattice parameters, Rietveld refinement analysis (Fig. 4) was performed by using *FULLPROF* software (Wyckoff, 1964) assuming *fm-3m* (225) space group for cubic type structure. Pseudo-voigt function was utilized to fit the various parameters to the data point (one scale factor, one zero shifting, four background, three cell parameters, five shape and width of the peaks, one global thermal factor and two asymmetric factors). Diamond software was utilized for extracting the possible packing diagram (Premkumar, Nagabhushana, Sharma, Daruka Prasad, et al., 2014) which is shown in inset of Fig. 4. The refined parameters such as occupancy, atomic functional positions are displayed in Table 1.The fitting parameters (R_p, R_{wp} and χ^2) indicate a good agreement between the refined and observed PXRD patterns for the cubic MgO phase.

The acceptable percentage difference in ionic radii between doped and substituted ions must not exceed 30%. The calculations of the radius percentage difference (D_r) between the doped ions (Fe^{3+}) and substituted ions (Mg^{2+}) in MgO: Fe^{3+} was calculated based on the formula (Fawad et al., 2014):

$$D_r = \frac{Rm(CN) - Rd(CN)}{Rm(CN)} \quad (7)$$

where, CN; co-ordination number, Rm (CN); Radius of host cations and Rd (CN); Radius of dopant ion and it was found that 12.5%. It was evident that the Fe^{3+} ionic radius was close to that of Mg^{2+} making it likely that Fe^{3+} ions would substitute with Mg^{2+} in the MgO host. Hence, it was believed that the Mg^{2+} sites were replaced by Fe^{3+} in this lattice.

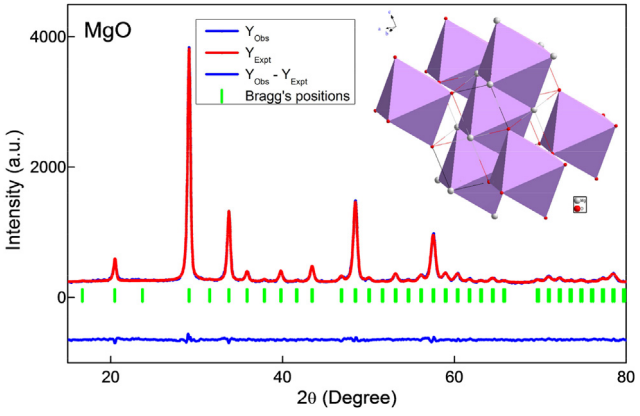

Fig. 4 – Rietveld refinement of MgO nanophosphor.

Table 1 – Rietveld refined structural parameters for MgO: Fe^{3+}.

Compounds	MgO
Crystal system	Cubic
Space group	Fm-3m (225)
Lattice parameters (Å)	
a = b = c	4.2305
$\alpha = \beta = \gamma$	90°
Unit cell volume (Å^3)	75.7148
Atomic coordinates	
Mg^{2+}	
x	0.00000
y	0.00000
z	0.00000
Occupancy	0.9879
Wyckoff notations	4a
O^{2-}	
x	0.50000
y	0.50000
z	0.50000
Occupancy	1.0390
Wyckoff notations	4b
Refinement parameters	
R_P	5.84
R_{WP}	7.85
R_{Exp}	7.86
$\chi 2$	0.999
R_{Bragg}	3.84
R_F	12.8
X-ray density (g/cc^3)	3.511

Fig. 5 shows the UV–Visible spectra for Fe^{3+} (1–9 mol %) doped MgO recorded in the wavelength region of 200–800 nm. In Fe^{3+} doped samples, the strong transmission peaks in the range 250–300 nm, along with broad transmittance at ~378 nm. The maximum transmittance (277 nm) may arise due to the transition between valence band to conduction band (Pan, Sun Chang, & Li, 2004). The weak transmittance in the UV–Visible region was expected due to extrinsic defects such as surface traps or defect states or impurities (Cao et al., 2004). For estimation of band gap in un-doped and Fe^{3+} doped MgO nanopowder, Wood and Tauc relation was used and the

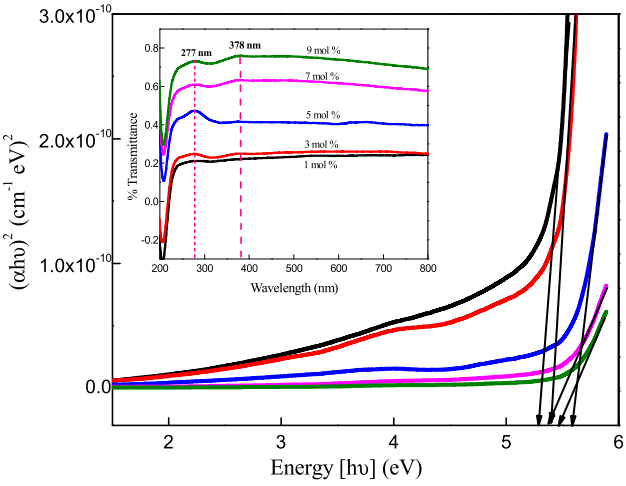

Fig. 5 – Uv–Vis absorption spectra of 1–9 mol % Fe^{3+} doped MgO.

details were given elsewhere (Tauc, 1970, Tauc, Grigorovici, & Vancu, 1966, Premkumar et al., 2012). The estimated band gap energy was found to be in the range of 5.3–5.6 eV. It was well known that two kinds of emission bands were observed in MgO crystals, in UV and visible region. The emission in the UV region was attributed to the recombination between electrons in conduction band and holes in valence band resulted from oxygen vacancies, which induce new energy levels and generate deep defect donors in the band gap. The visible emission was related to the defects related deep level emission such as oxygen vacancies and Mg interstitials. Therefore, high oxygen vacancies in our samples may preferentially occur during the sample preparation via combustion synthesis. The emission peaks in the range 300–450 nm (3.14 eV, bluish-violet region) was attributed to surface defects namely oxygen vacancies, F-centers (oxygen ion vacancy occupied by two electrons)/F^+-centers (oxygen ion vacancy occupied by single electrons)/surface states of the host material. The emission intensity in combustion derived sample was mainly due to the presence of higher density of defects present on the surface of nanoparticles (Changhyun, Kim, Park, & Lee, 2012, Yanagida, Nagashima, Tanaka, & Kawai, 2008).

Fig. 6 shows the Fourier transform infrared (FTIR) spectra of undoped and MgO: Fe^{3+} (1–9 mol %) samples. The strong band at 498 cm^{-1} was associated with the characteristic vibrational mode of symmetric MgO_6 octahedral of MgO. Further, the peak at 550-890 cm^{-1} (γ_1) higher frequency of MgO stretching and 410-450 cm^{-1} (γ_2) is lower frequency stretching. The peak at 886 cm^{-1} is attributed to Mg–O–Mg interactions. The absorption in the range of 1300–1800 cm^{-1} related to hydroxyl group of molecular water at 1635 cm^{-1}, NH_3 at 1440 cm^{-1} and it was due to C=O stretching mode. The peak at ~2376 cm^{-1} arises due to absorption of atmospheric CO_2 on the metallic cations. Also, the absorption at ~3445 cm^{-1} indicates the presence of hydroxyl groups (O–H mode), which was probably due to the fact that the spectra was not recorded in situ and some water re-adsorption from the ambient atmosphere as occurred (Selvamani, Yagyu, Kawasaki, & Mukhopadhyay, 2010, Borghei, Kamali, Shakib, Bazrafshan, & Ghoranneviss, 2011).

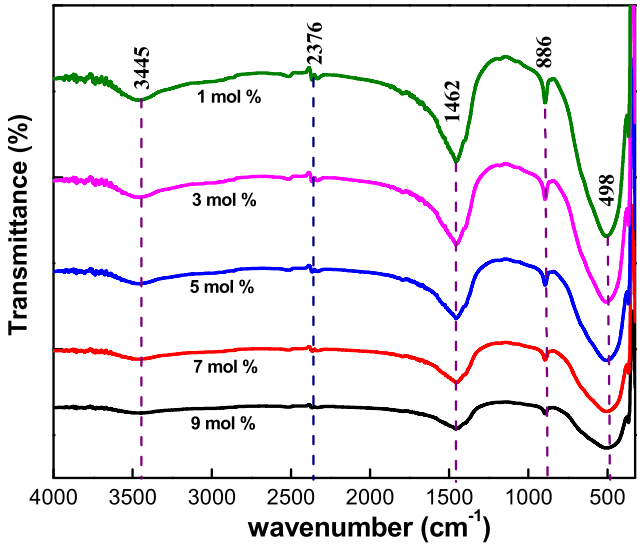

Fig. 6 – FTIR spectra of 1–9 mol % Fe^{3+} doped MgO nanophosphor.

Electron microscopy is a versatile tool capable of providing structural information over a wide range of magnification. Further, Texture, topography and surface features of the nanophosphors were characterized by SEM. It was clearly observed from SEM pictures of MgO: Fe^{3+} samples prepared via combustion technique as shown in Fig. 7 (A–D). The powders show hollow sphered morphology with porous and large agglomerates of very fine particles. The SEM results reveal that the powder was porous and agglomerated with poly-crystalline nanoparticles. It was well known that, combustion synthesis reaction was influenced by metal–ligand complex formation. Depending upon the type of fuel and metal ions, the nature of combustion differs from flaming (gas phase) to non-flaming (smoldering and heterogenous) type. Generally, flaming reactions involve liberation of large quantity of gas. The pores and voids were attributed to the large amount of gases escaping out of the reaction mixture during combustion (Chandrasekhar et al., 2014; Sunitha et al., 2012). It was confirmed that the dopant concentration does not influence the morphology of the sample. TEM studies were carried out to understand the crystalline characteristics of the nanoparticles. Fig. 8(A–D) illustrates the TEM images of pure MgO nanoparticles. The particles were observed to be irregular shaped and highly dispersed and the size was found to be in the range 5–10 nm. The selected area electron diffraction (SAED) image showed distinct ring pattern which was an evidence for the polycrystalline behavior of the as-prepared nanoparticles (Venkata Reddy et al., 2012). Further, a well defined lattice fringes obtained by high resolution TEM (HRTEM) pattern reveals the formation of highly crystalline pure MgO nanophosphors (Shivram et al., 2014). As seen in the spacing between the adjacent lattice fringes of the nanoparticles was 0.253 nm, which was very close to that of 0.245 nm for MgO. The composition of obtained MgO was analyzed by means of energy dispersive X-ray analysis (EDX) as shown in Fig. 8(D). The EDX result showed the presence of Mg and O by the appearance of Mg and O peaks without any other characteristic peaks confirms the purity of the sample.

Photoluminescence (PL) spectroscopy is an important tool to characterize the optical properties of a semiconductor. PL intensity may be directly correlated with the defect density in a nano material. The excitation spectra of Fe^{3+} doped MgO monitored at 720 nm emission was shown in Fig. 9. The PL Excitation bands obtained at 378, 419, 438, 450 and 467 nm and the excitation intensity maximum was located at 378 nm.

In the excitation spectrum of the Fe^{3+} doped MgO, the strong absorption band observed at 378 nm due to the transitions of $^6A_1(^6S) \rightarrow {}^4E(^4G)$ on the Fe^{3+} ion of the emission at 718 nm. On excitation using 378 nm band, emission band was observed around 718 nm, with superimposed bands at 513 and 618 nm. The ground state term of this configuration was $^6A_1$ (^6S). Ground state was the only sextet of d^5 configuration; hence all the electronic transitions are spin forbidden. In a cubic field approximation, the free electron term ^4G splits up into $^4T_1(^4G)$; $^4T_2(^4G)$ and the degenerate $^4A_1$; $^4E(^4G)$. The ground state free-ion term which transforms to $^6A_1$ (^6S) was a horizontal line. Also, the $^4E(^4G)$; $^4A_1(^4G)$; $^4E(^4D)$ and $^4A_2(^4D)$ terms are horizontal so that their energies are independent of the

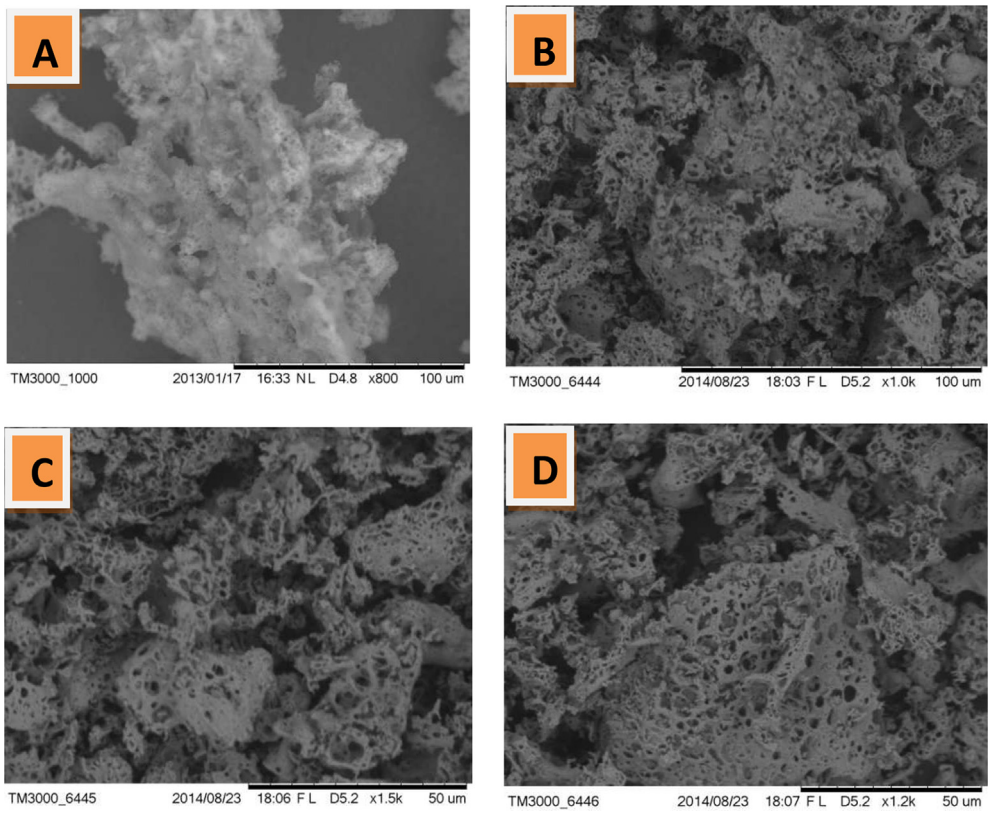

Fig. 7 – SEM images of A) un-doped B) 1 mol % C) 5 mol % D) 9 mol % doped MgO.

crystal field. Since the slope of the ground state term $^6A_1(6S)$ was zero and the slope of the $^4E(^4G)$; $^4A_1(^4G)$; $^4E(^4D)$ and $^4A_2(^4D)$ terms were also zero, transitions from ground state to these four states should give rise to sharp peaks. By the same reasoning the transitions to states which slope appreciably such as $^4T_1$ and $^4T_2$ give broader bands. Hence the excitation bands observed can be assigned as follows: $^6A_1(6S) \rightarrow {}^4E(^4G)$ or $^6A_1(^6S) \rightarrow {}^4A_1(^4G)$in the range 378 and 400 nm, $^6A_1(6S) \rightarrow {}^4T_2(^4G)$ 576 nm (Nayak & Kutty, 1998).

PL study gives us the fundamental information about energy levels lying within the band gap states. The PL emission infers the efficacy of charge carrier trapping, migration and also the fate of photo generated electron–hole pairs in the materials. The recombination of excited electron–hole pair was the result of PL emission and hence efficient charge carrier separation resulted in lower PL intensity.

Photoluminescence emission spectra for MgO: Fe^{3+} (1–9 mol %) sample excited with UV light source (378 nm) at room temperature (RT) were recorded and as shown in Fig. 10. The lower energy band at 720 nm and the intermediate band located at 618 nm was attributed to $^4T_1$ (4G) → $^6A_1$ (6S) and $^4T_2$ (4G) → $^6A_1$ (6S) transitions respectively (Premkumar et al., 2014). The higher energy band located at 513 nm was associated to $^4E + {}^4A_1$ (^4G) → $^6A_1$ (^6S) transitions of Fe^{3+} ions. Pedro et al. (Pedro, Nakamura, Barthem, & Sosman, 2009) studied PL of the Fe^{3+} doped $LiGa_5O_8$–$LiGaSiO_4$–$Li_5GaSi_2O_8$ glasses and observed the luminescence bands in the red region of the visible spectrum. The Fe^{3+} emissions from higher excited states (in blue–green region) were seldom, but were observed recently for both tetrahedral and octahedral sites (Bingham, Parker, Searle, & Smith, 2007). The observed spectra were associated with spin-forbidden transitions of Fe^{3+} tetrahedrally coordinated by O^{2-} ligand anions.

In MgO nanostructures, the presence of defects was due to appreciable bond breaking and surface stress caused by large surface to volume ratio. These defects may convert F^+ and F centers to F-aggregates namely F_2, F^{2+}, F_2^{2+}. The weak emission bands at 532 nm may also results from the host material and might be due to oxygen vacancy. It was caused due to singlet to singlet or singlet to triplet transitions. Therefore, the emission comes mainly from radiative recombination of the large amount of trapped carriers excited from MgO (Biswajit Choudhury, Basyach, & Choudhury, 2014; Kumar & Kumar, 2008; Kumar, Thota, Varma, Kumar, 2011; Lin et al., 2008).

When Fe^{3+} ions were doped into the host, they could probably occupy octahedral sites. It is suggested that only a minor fraction of the total amount of Fe^{3+} goes into Mg^{2+} substitution sites and a larger amount may be precipitated into MgO: Fe^{3+} clusters, or even separated as a metal oxide phase. The excess amount of Fe_2O_3 will likely reside on either surface or grain boundaries of the nanocrystals to yield optimum strain relief. In the present study no PXRD peaks from Fe_2O_3 ($2\theta = 33.2^\circ$ or 35.6°) (Cao et al., 2005) detected even at 9 mol % indicating that Fe^{3+} ions enter into the host lattice and replace magnesium ion located on the surface of the nanocrystals because of the porosity of MgO. Therefore, Fe^{3+} ions in the MgO structure exhibit a bright red emission at 720 nm. MgO is an insulator, has high physical and chemical stability,

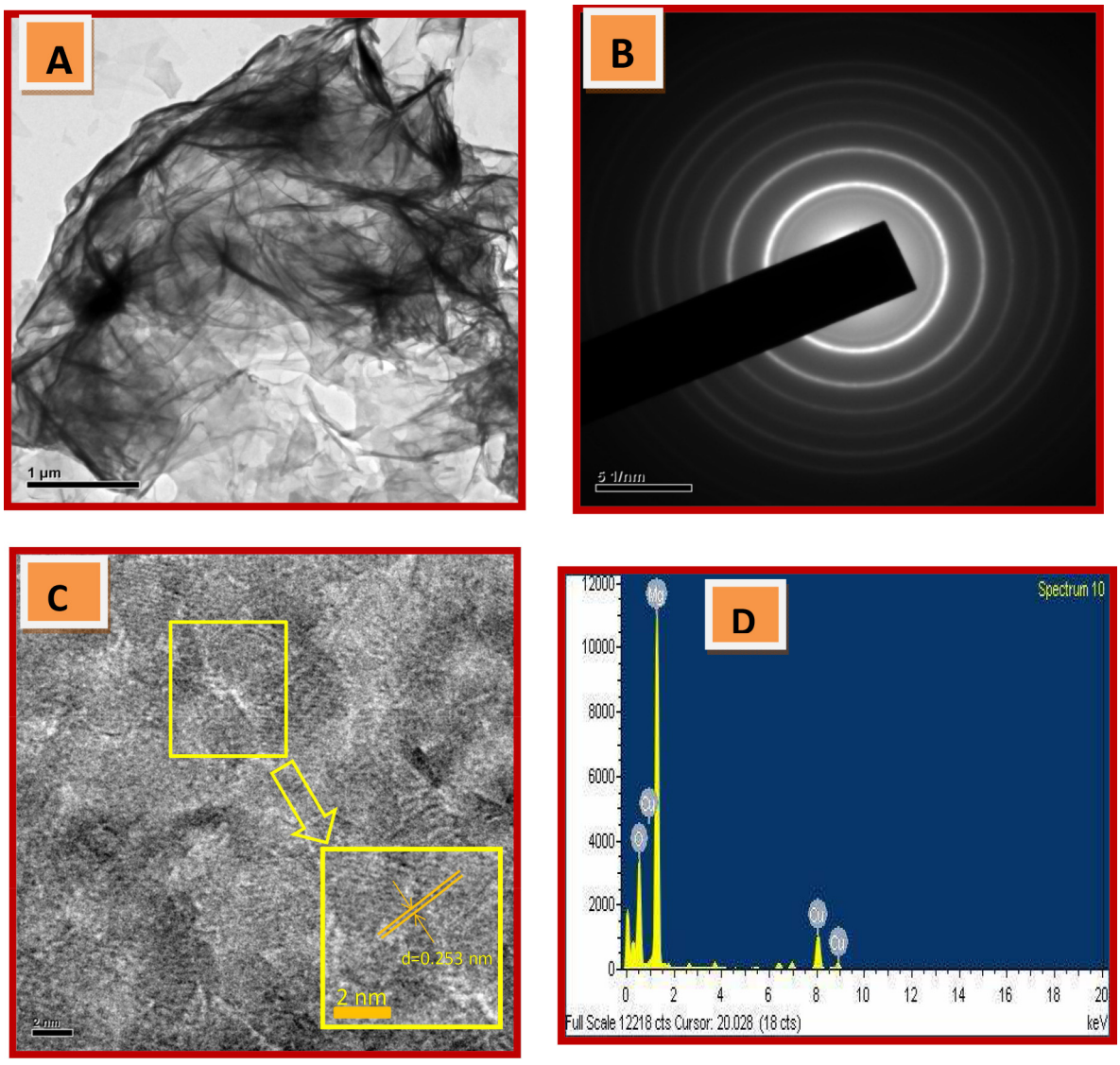

Fig. 8 – (A–D). TEM, SAED, HRTEM and EDAX of MgO nanopowders.

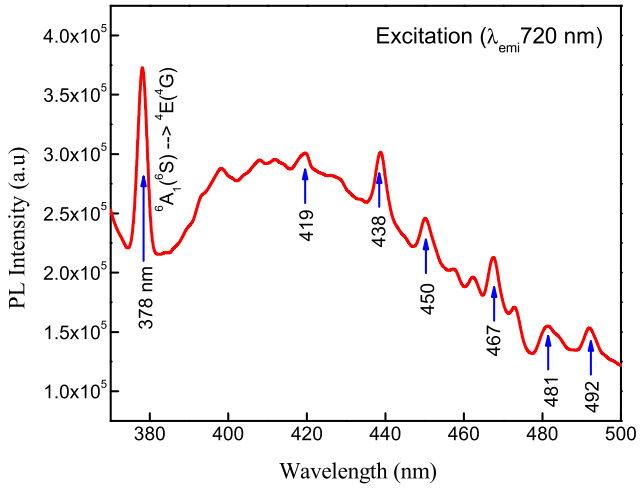

Fig. 9 – Excitation spectra of MgO: Fe^{3+} nanophosphor emission centered at 718 nm.

poor desiccant, due to its high melting point used as a refractory. Also, it was used as a reference white color owing to its good diffusing and reflectivity properties (Telex Peter & Waldron, 1955). MgO has a rocksalt structure (fcc) with magnesium ions occupying octahedral sites within the anion closed packed structure. Its ionic constituents comprise a relatively small number of electrons, its nanostructures were expected to have novel properties superior to their bulk counterparts due to the large surface to volume ratio effect of nanocrystals (Yang & Kim, 2004). The Mg atoms were present at the corner of the cube and are coordinated by eight equivalent-nearest neighbor oxygen atoms. In this lattice, the point group symmetry of Mg sites in the cubic MgO structure was ideally D_{2d} and Mg site possesses inversion symmetry. When Fe^{3+} ions were doped into the host, they could probably occupy these sites. Owing to the different charge for the cations, oxygen vacancies were formed to balance the charge difference. The excess amount of Fe_2O_3 will likely reside on

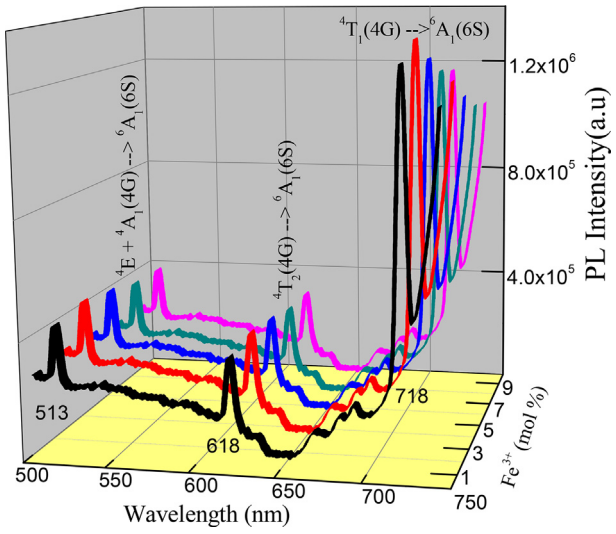

Fig. 10 – PL spectrum of MgO: Fe^{3+} (1–9 mol %) nanophosphors recorded at room temperature (λ_{exc} - 378 nm).

either surface or grain boundaries of the nanocrystals to yield optimum strain relief. The defect reaction equation can be represented in the following way,

$$\left(1-x\right)MgO + 0.5xFe_2O_3 = xFe'_{Ce} + 0.5xV''_O + (1-x)Mg^x_{Mg} + (2-0.5x)O^x_o \quad (8)$$

where 'Fe'_{Ce}' means 'Fe' occupying the site normally occupied by a 'Mg^{2+}' due to replacement by 'Fe', 'V''_O' is the 'O^{2-}' vacancy, 'Mg^x_{Mg}' represents the rest magnesium in the lattice of MgO, and 'O^x_o' was the oxygen in the lattice of MgO (Shi, Hossu, Hall, & Chen, 2012).

To optimize the doping concentration for efficient luminescence, the concentration of Fe^{3+} ions in MgO phosphor was varied from 1 to 9 mol %. The variation of PL intensity with Fe^{3+} concentration was shown in Fig. 11A. The figure illustrates that, the luminescence intensities at 513 nm, 618 nm and 718 nm of the MgO: Fe^{3+} phosphors increases with the increase of Fe^{3+} ion concentration, reaches a maximum for 3 mol % of Fe^{3+} and then decreases with further increase of concentration due to energy transfer among the excited Fe^{3+} ions at higher concentrations and also due to concentration quenching. As dopant concentration of Fe^{3+} increases, $^4T_2$ (4G) → $^6A_1$ (6S) transition dominates and the emission intensity increases. This may be attributed to the increase distortion of the local field around the Fe^{3+} ions. Moreover, there was charge imbalance in the host lattice due to doping of trivalent Fe^{3+} cations. The reason must be that when the concentration of Fe^{3+} continues to increase, the interaction between the dopant ions increases, leads to self-quenching and thereby PL intensity decreases (Viagin, Masalov, Ganina, & Malyukin, 2009).

The concentration quenching might be explained on the basis of the following two factors: (i) the excitation migration due to resonance between the activators was enhanced when the doping concentration was increased, and thus the excitation energy reaches quenching centers, and (ii) the activators were paired or coagulated and were changed to quenching centers. The energy can also be transferred non-radiatively by the radiative reabsorption or multipole–multipole interaction (Chen, Ma, Zhang, & Li, 2009; Naik, Prashantha, Nagabhushana, Nagaswarupa, et al., 2014; Naik, Prashantha, Nagabhushana, Sharma, et al., 2014). Also, the increase in Fe^{3+} concentration can result in cross-relaxation processes in close Fe^{3+}–Fe^{3+} pairs, the quenching of Fe^{3+} luminescence often occurs at low concentration.

Fe_2O_3 does not show PL emission in its bulk form due to the local d-band transition nature and efficient energy relaxation (Han et al., 2007). In nanosized particles the increase of Fe–O bonding separation, resulting in enhancement of the magnetic coupling of the neighboring Fe^{3+}, which was responsible for PL (Blake, Hessevick, Zoltai, & Finger, 1966). Zou et al. (Zou & Volkov., 2000) investigated the optical spectral characteristics of the chemically synthesized iron oxide nanocrystals with different sizes. They observed the different optical responses in different energy and time scales, from local d–d

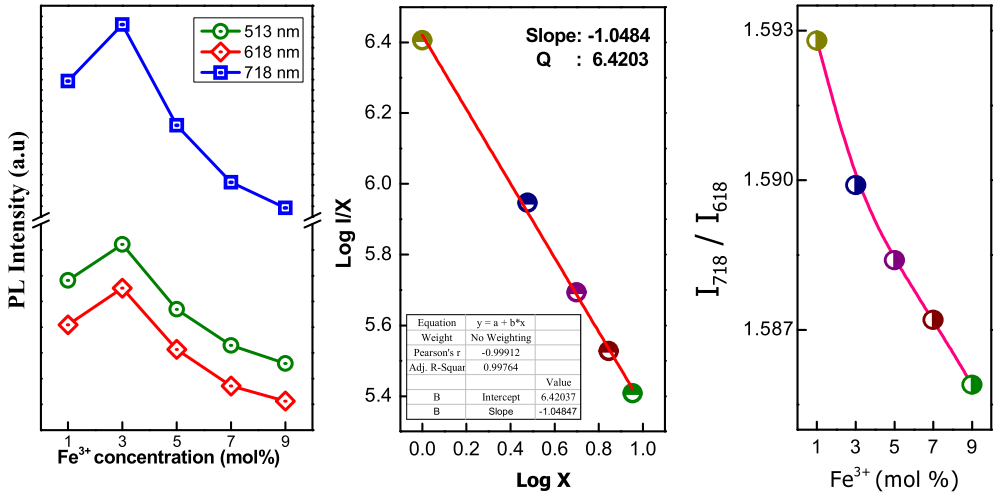

Fig. 11 – Variation of PL intensity, Relation between log(x) and log (I/x) and asymmetric ratio of MgO: Fe^{3+} (1–9 mol %) nanophosphor Fe^{3+} concentration.

transitions to delocalized pair excitations and charge-transfer transitions by the femtosecond time-resolved absorption spectra. They observed that the emission peak position and the PL intensity was significantly affected by the nanocrystalline size and surface morphology.

The energy transfer mechanism in phosphors was essential in order to obtain the critical distance (Rc) i.e. the critical separation between Fe^{3+} and the quenching site was calculated according to the equation given by Blasse & Bril (1967).

$$R_c \approx 2\left[\frac{3V}{4\pi X_c N}\right]^{1/3} \tag{9}$$

where X_c; the critical concentration, N; the number of cation sites in the unit cell, and V; the volume of the unit cell. For MgO: Fe^{3+} nanophosphor the values of N, V and Xc were 4, 74.78 $Å^3$ and 0.03 respectively. The estimated 'R_c' was found to be 10.59 Å. Since 'R_c' is not less than 5 Å, exchange interaction is not responsible for non radiative energy transfer process from one Fe^{3+} ion to another Fe^{3+} ion in this host. According to Blasse theory (Blasse, 1969), the non radiative transfer between different Fe^{3+} ions in MgO phosphor may occur by radiative re-absorption/exchange interaction/multipole–multipole interaction.

Therefore, multipolar interaction was used to explain the concentration quenching mechanism. Multipolar interaction involves several types of interaction such as dipole–dipole (d–d), dipole-quadropole (d-q), quadropole–quadropole (q–q) interaction. As a result, the energy transfer process of Fe^{3+} in MgO phosphor would be due to multipolar interaction (Devaraj et al., 2014). In order to determine the type of interaction involved in the energy transfer Vanuitert's (Van Uitert, 1967) proposed an equation:

$$\frac{I}{X} = k\left[1+\beta(X)^{Q/3}\right]^{-1} \tag{10}$$

where I; the integral intensity of emission spectra from 450 to 740 nm, X; the activator concentration, I/X; the emission intensity per activator (X), β and K; constants for a given host under same excitation condition. According to above equation, Q = 3 for the energy transfer among the nearest neighbor ions, while Q = 6, 8 and 10 for d–d, d-q and q–q interactions respectively (R. Naik, Prashantha, Nagabhushana, Nagaswarupa, et al., 2014; Naik, Prashantha, Nagabhushana, Sharma, et al., 2014, Fu Yang et al., 2013). Assuming that $\beta(X)^{Q/3} >> 1$, above equation can be written as

$$\log\left(\frac{I}{X}\right) = K' - \left(\frac{Q}{3}\right)\log X (K' = \log K - \log \beta) \tag{11}$$

From Equation (11), the multipolar character (Q) can be obtained by plot log (I/X) v/s log (X) as shown in Fig. 11B. The slope and multipolar character 'Q' was found to be ~ −1.0484 and 6.4203 which was close to 6. Therefore, the concentration quenching in MgO: Fe^{3+} phosphor occurred due to dipole to dipole interaction.

Further, the intensity ratio of ED and MD (Asymmetry ratio, A_{21}) transitions were used to measure the symmetry of the local environment of the trivalent 4f ions which was sensitive to the nature of the Fe^{3+} ions in the host lattice (Wang, Chen, et al., 2012; Wang, Li, et al., 2012, Dhananjaya et al., 2011). This gives a measure of the degree of distortion from inversion symmetry of the local environment surrounding the Fe^{3+} ions in the host matrix.

$$A_{21} = \frac{\oint I_2(^4F_{9/2} \rightarrow {}^6H_{13/2})d\lambda}{\oint I_1(^4F_{9/2} \rightarrow {}^6H_{15/2})d\lambda} \tag{12}$$

Where I_2; intensity at 718 nm $^4T_1$ (4G) → $^6A_1$ (6S) and I_1; intensity at 618 nm $^4T_2$ (4G) → $^6A_1$ (6S). The values of A_{21} decrease with increase of Fe^{3+} ions. However, it was reasonable to believe that the doping of Fe^{3+} will introduce lattice defects, which will undoubtedly reduce the symmetry strength of the local environment of Mg^{2+} sites (Sunitha et al., 2012). Consequently, the symmetry ratio of the sample doped with rare earth cations decreases with the increase of dopant concentration and as shown in Fig. 11C.

The Commission International De I-Eclairage (CIE) chromaticity coordinates (Naik, Prashantha, Nagabhushana, Nagaswarupa, et al., 2014; Naik, Prashantha, Nagabhushana, Sharma, et al., 2014, Premkumar et al., 2014) for MgO: Fe^{3+} (1–9 mol %) phosphors was calculated with respect to Fe^{3+} concentration (Fig. 12A). The CIE coordinates of white emission of Fe^{3+} ions not only depend upon the asymmetric ratio but also depend upon the higher energy emission levels. Co-ordinated color temperature can be estimated by Planckian locus, which is only a small portion of the (x, y) chromaticity diagram and there exist many operating points outside the Planckian locus. If the coordinates of a light source do not fall on the Planckian locus, the coordinated color temperature (CCT) was used to define the color temperature of a light source. CCT was calculated by transforming the (x, y) co-ordinates of the light source to (U′, V′) by using following equations, and by determining the temperature of the closest point of the Planckian locus to the light source on the(U′, V′) uniform chromaticity diagram (Fig. 12B) (Judd, 1936, Schanda & Danyi, 1977).

$$U' = \frac{4x}{-2x+12y+3} \tag{13}$$

$$V' = \frac{9y}{-2x+12y+3} \tag{14}$$

It was observed that the CIE co-ordinates of Fe^{3+} activated MgO: Fe^{3+} phosphor was very close to the National Television System Committee (NTSC) standard values, they fall close to the white region of chromaticity diagram and their corresponding location was marked with star in white region. Also, CCT was found to be 4766 K using U′ = 0.20295 and V′ = 0.50589. Therefore, the present phosphor was quite useful for the production of artificial white light to be similar to those of natural white light owing to its better spectral overlap in white LEDs and in solid state display applications.

4. Conclusion

In the present work, MgO: Fe^{3+} (1–9 mol %) nanophosphors were prepared by simple and low cost solution combustion method at low temperature (400 °C). The PXRD patterns confirmed single phase, cubic structure and the particle size

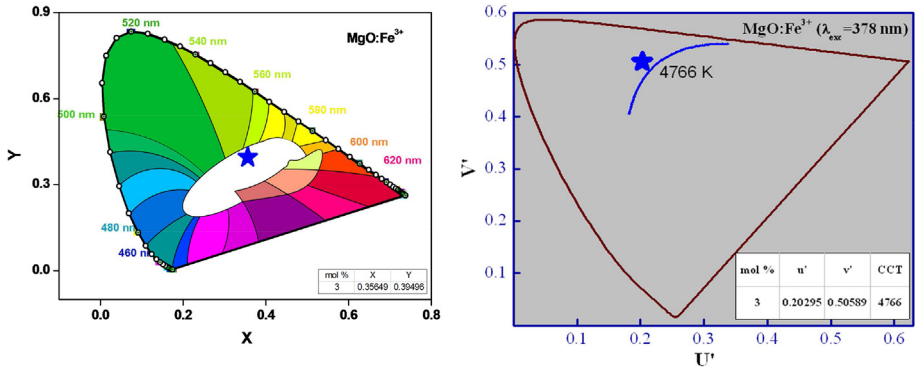

Fig. 12 – CIE chromaticity and CCT diagram of MgO: Fe^{3+} (3 mol %) nanophosphor.

is in nano range confirmed by TEM. The UV-Vis absorption of doped phosphor show an intense absorption band in the range 300–400 nm corresponding to ligand-to-metal charge-transfer (O^{2-} to Fe^{3+}) band. SEM results confirm the porous nature of the sample. Upon excitation at 378 nm characteristic photoluminescence (PL) peaks recorded at ~ 513 [$^4E + {}^4A_1$ (^4G) → $^6A_1$ (^6S)], ~618 [$^4T_2$ (4G) → $^6A_1$ (6S)] and ~720 nm [$^4T_1$ (4G) → $^6A_1$ (6S)]. Further, the peak at 720 nm exhibit strong red emission and can be applied to the red emission of phosphor for the application for (NUV) excitation. It was observed that the emission spectrum excited at 378 nm showed prominent spectral lines with higher order of intensity. Further, the phosphor showed excellent CIE chromaticity co-ordinates (x, y) and CCT as a result it was quite useful for display and solid state light applications.

Acknowledgments

The authors PBD, SCP and HPN thanks to VGST, Govt. of Karnataka, India, (No: VGST/CISEE/2013-14/282) and (No: VGST/K-FIST-L1/2014-15/360) for extended to carry out this research work. One of the author HN thanks to DST nano mission for funding of research project to Center for Nano Research, Tumkur University, Tumkur for extended to carry out this research work.

REFERENCES

Adamski, A., Wałesa-Chorab, M., Kubicki, M., Hnatejko, Z., & Patroniak, V. (2014). Absorption spectra, luminescence properties and electrochemical behavior of Mn(II), Fe(III) and Pt(II) complexes with quaterpyridine ligand. *Polyhedron, 81*, 188–195.

Bingham, P. A., Parker, J. M., Searle, T. M., & Smith, I. (2007). Local structure and medium range ordering of tetrahedrally coordinated Fe^{3+} ions in alkali-alkaline earth-silica glasses. *Journal of Non-Crystalline Solids, 353*, 2479–2494.

Blake, R. L., Hessevick, R., Zoltai, T., & Finger, L. (1966). Refinement of the hematite structure. *American Mineralogist, 51*, 123–129.

Blasse, G. (1969). Energy transfer in oxidic phosphors. *Philips Research Reports, 24*, 131–144.

Blasse, G., & Bril, A. (1967). A new phosphor for flying-spot cathode-ray tubes for color television: yellow-emitting $Y_3Al_5O_{12}:Ce^{3+}$. *Applied Physics Letter, 11*, 53–55.

Borghei, S. M., Kamali, S., Shakib, M. H., Bazrafshan, A., & Ghoranneviss, M. J. (2011). Filament temperature dependence of the nano-size MgO particles prepared by the HWCVD technique. *Journal of Fusion Energy, 30*, 433–436.

Cao, M. H., Gao, S., Sun, G. B., Wu, X. L., Hu, C. W., & Wang, Z. L. (2005). Single-Crystal dendritic micro-pines of magnetic α-Fe_2O_3: large-scale synthesis, formation mechanism, and properties. *Angewandte Chemie International Edition, 44*, 4197–4201.

Cao, H. Q., Qiu, X. Q., Luo, B., Liang, Y., Zhang, Y. H., Tan, R. Q., et al. (2004). Synthesis and room-temperature ultraviolet photoluminescence properties of zirconia nanowires. *Advanced Functional Materials, 14*, 243–246.

Chandrasekhar, M., Nagabhushana, H., Sharma, S. C., Sudheer kumar, K. H., Dhananjaya, N., Sunitha, D. V., et al. (2014). Particle size, morphology and color tunable ZnO: Eu^{3+} nanophosphors via plant latex mediated green combustion synthesis. *Journal of Alloys and Compounds, 584*(25), 417–424.

Changhyun, J., Kim, H., Park, S., & Lee, C. (2012). Synthesis of biaxial MgO/Mg–Sn–O nanowire heterostructures and their structural and luminescence properties. *Journal of Alloys and Compounds, 541*, 163–167.

Chen, X. Y., Ma, C., Zhang, Z. J., & Li, X. X. (2009). Structure and photoluminescence study of porous red-emitting $MgAl_2O_4:Eu^{3+}$ phosphor. *Microporous and Mesoporous Materials, 123*, 202–208.

Choudhury, B., Basyach, P., & Choudhury, A. (2014). Monitoring F, F^+ and $F^{2,2+}$ related intense defect emissions from nanocrystalline MgO. *Journal of Luminescence, 149*, 280–286.

Devaraja, P. B., Avadhani, D. N., Nagabhushana, H., Prashantha, S. C., Sharma, S. C., Nagabhushana, B. M., et al. (2014). MgO: Dy^{3+}nanophosphor: self ignition route, characterization and its photoluminescence properties. *Materials Characterization, 97*, 27–36.

Devaraja, P. B., Avadhani, D. N., Prashantha, S. C., Nagabhushana, H., Sharma, S. C., Nagabhushana, B. M., et al. (2014a). *Spectrochimica Acta Part A: Molecular and Biomolecular Spectroscopy, 118*, 847–851.

Devaraja, P. B., Avadhani, D. N., Prashantha, S. C., Nagabhushana, H., Sharma, S. C., Nagabhushana, B. M., et al. (2014b). MgO: Eu^{3+} red nanophosphor: low temperature synthesis and photoluminescence properties. *Spectrochimica Acta Part A: Molecular and Biomolecular Spectroscopy, 121*, 46–52.

Dhananjaya, N., Nagabhushana, H., Nagabhushana, B. M., Rudraswamy, B., Shivakumara, C., & Chakradhar, R. P. S.

(2011). Effect of Li(+) – ion on enhancement of photoluminescence in Gd2O3:Eu^{3+} nanophosphors prepared by combustion technique. *Journal of Alloys and Compounds, 509*, 2368–2374.

Fawad, U., Oh., M., Park, H., Kim, S., & Kim, H. J. (2014). Luminescent investigations of $Li_6Lu(BO_3)_3$:Tb^{3+}, Dy^{3+} phosphors. *Journal of Alloys and Compounds, 610*, 281–287.

Gu, F., Li, C., Cao, H., Shao, W., Hu, Y., & Chen, J. (2008). Crystallinity of Li-doped MgO: Dy^{3+} nanocrystals via combustion process and their photoluminescence properties. *Journal of Alloys and Compounds, 453*, 361–365.

Han, Q., Liu, Z. H., Xu, Y. Y., Chen, Z. Y.., Wang, T. M., & Zhang, H. (2007). Growth and properties of single-crystalline gamma-Fe_2O_3 nanowires. *Journal of Physics Chemistry, C. 111*, 5034–5038.

Jayalakshmi, M., & Balasubramanian, K. (2009). Solution combustion synthesis of Fe_2O_3/C, Fe_2O_3-SnO_2/C, Fe_2O_3-ZnO/C Composites and their electrochemical characterization in non-aqueous electrolyte for supercapacitor application. *International Journal of Electrochemical Science, 4*, 878–886.

Judd, D. B. (1936). Estimation of chromaticity differences and nearest color temperature on the standard 1931 ICI colorimetric coordinate system. *Journal of Optical Society of America, 26*, 421–426.

Kijima, N., Yoshinaga, M., Awaka, J., & Akimoto, J. (2011). Microwave synthesis, characterization, and electrochemical properties of Fe_2O_3 nanoparticles. *Solid State Ionics, 192*, 293–297.

Kumar, A., & Kumar, J. (2008). On the synthesis and optical absorption studies of nano-size magnesium oxide powder. *Solid State Communication, 147*, 405–408.

Kumar, N., Sanyal, D., & Sundaresan, A. (2009). Defect induced ferromagnetism in MgO nanoparticles studied by optical and positron annihilation spectroscopy. *Chemical Physics Letters, 477*, 360–364.

Kumar, A., Thota, S., Varma, S., & Kumar, J. (2011). Sol-gel synthesis of highly luminescent magnesium oxide nanocrytallites. *Journal of Luminescence, 131*, 640–648.

Lakshminarasappa, B. N., Prashantha, S. C., & Singh, F. (2011). Ionoluminescence studies of combustion synthesized Dy^{3+} doped nano crystalline forsterite. *Current Applied Physics, 11*, 1274–1277.

Lin, L., Yin, M., Shi, C., & Zhang, W. (2008). Luminescence properties of a new red long-lasting phosphor: Mg_2SiO_4:Dy^{3+}, Mn^{2+}. *Journal of Alloys and Compounds, 455*, 327–330.

Malleshappa, J., Nagabhushana, H., Sharma, S. C., Prashantha, S. C., Dhananjaya, N., Shivakumara, C., et al. (2014). Eco-friendly green synthesis, structural and photoluminescent studies of CeO_2:Eu^{3+} nanophosphors using *E. tirucalli* plant latex. *Journal of Alloys and Compounds, 612*, 425–434.

Maoz, B. M., Tirosh, E., Bar Sadan, M., & Markovich, G. (2011). Defect-induced magnetism in chemically synthesized nanoscale sheets of MgO. *Physical Review B, 83*, 161–201.

Moyses Araujo, C., Kapilashrami, M., Jun, X., Jayakumar, O. D., Nagar, S., Wu, Y., et al. (2010). Room temperature ferromagnetism in pristine MgO thin films. *Applied Physics Letters, 96*, 232505.

Nagabhushana, H., Sunitha, D. V., Sharma, S. C., Prashantha, S. C., Nagabhushana, B. M., & Chakradhar, R. P. S. (2014). $CdSiO_3$:Eu^{3+} red nanophosphors prepared by low temperature solution combustion technique, its structural and luminescent properties. *Journal of Alloys and Compounds, 616*, 284–292.

Naik, R., Prashantha, S. C., Nagabhushana, H., Nagaswarupa, H. P., Anantharaju, K. S., Sharma, S. C., et al. (2014). Mg_2SiO_4:Tb^{3+} nanophosphor: auto ignition route and near UV excited photoluminescence properties for WLEDs. *Journal of Alloys and Compounds, 617*, 69–75.

Naik, R., Prashantha, S. C., Nagabhushana, H., Sharma, S. C., Nagabhushana, B. M., Nagaswarupa, H. P., et al. (2014). Low temperature synthesis and photoluminescence properties of red emitting Mg_2SiO_4:Eu^{3+} nanophosphor for near UV light emitting diodes. *Sensors and Actuators B: Chemical, 195*, 140–149.

Nayak, M., & Kutty, T. R. N. (1998). Luminescence of Fe^{3+} doped $NaAlSiO_4$ prepared by gel to crystallite conversion. *Material Chemistry and Physics, 57*, 138–146.

Orante-Barro, V. R., Oliveira, L. C., Kelly, J. B., Milliken, E. D., Denis, G., Jacobsohn, L. G., et al. (2011). Luminescence properties of MgO produced by solution combustion synthesis and doped with lanthanides and Li. *Journal of Luminescence, 131*, 1058–1065.

Pan, L. K., Sun Chang, Q., & Li, C. M. (2004). Elucidating Si–Si dimmer vibration from the size-dependent Raman shift of nanosolid Si. *Journal of Physics and Chemistry, B, 108*, 3404–3407.

Pedro, S. S., Nakamura, O., Barthem, R. B., & Sosman, L. P. (2009). Photoluminescence and photoacoustic spectroscopies of Fe3+ in the $LiGa_5O_8$–$LiGaSiO_4$–$Li_5GaSi_2O_8$ system. *Journal of Fluorescence, 19*, 211–219.

Prashantha, S. C., Lakshminarasappa, B. N., & Singh, F. (2012). 100 MeV Si8+ ion induced luminescence and thermoluminescence of nanocrystalline Mg_2SiO_4:Eu^{3+}. *Journal of luminescence, 132*, 3093–3097.

Premkumar, H. B., Nagabhushana, H., Sharma, S. C., Daruka Prasad, B., Nagabhushana, B. M., Rao, J. L., et al. (2014). Synthesis, EPR and luminescent properties of $YAlO_3$:Fe^{3+} (0.1–0.9 mol %) nanopowders. *Spectrochimica Acta Part A: Molecular and Biomolecular Spectroscopy, 126*, 220–226.

Premkumar, H. B., Nagabhushana, H., Sharma, S. C., Prashantha, S. C., Nagaswarupa, H. P., Nagabhushana, B. M., et al. (2014). Structural, photo and thermoluminescence studies of Eu^{3+} doped orthorhombic $YAlO_3$ nanophosphors. *Journal of Alloys and Compounds, 601*, 75–84.

Premkumar, H. B., Ravikumar, B. S., Sunitha, D. V., Nagabhushana, H., Sharma, S. C., Savitha, M. B., et al. (2013). Investigation of structural and luminescence properties of Ho^{3+} doped $YAlO_3$ nanophosphors synthesized through solution combustion route. *Spectrochimica Acta Part A: Molecular and Biomolecular Spectroscopy, 115*, 234–243.

Premkumar, H. B., Sunitha, D. V., Nagabhushana, H., Sharma, S. C., Nagabhushana, B. M., Rao, J. L., et al. (2012). $YAlO_3$:Cr^{3+} nanophosphor: synthesis, photoluminescence, EPR, dosimetric studies. *Spectrochimica Acta Part A: Molecular and Biomolecular Spectroscopy, 96*, 154–162.

Ren, C., Sun, J., Li, J., Chen, X., Hu, Z., & Xue, D. (2009). Bi-functional silica nanoparticles doped with iron oxide and CdTe prepared by a Facile method. *Nanoscale Research Letter, 4*, 640–645.

Schanda, J.., & Danyi, M. (1977). Correlated color-temperature calculations in the CIE 1976 chromaticity diagram. *Color Research & Application (Wiley Interscience), 2*, ,161–163.

Selvamani, T., Yagyu, T., Kawasaki, S., & Mukhopadhyay, I. (2010). Easy and effective synthesis of micrometer-sized rectangular MgO sheets with very high catalytic activity. *Catalysis Communications, 11*, 537–541.

Shi, S., Hossu, M., Hall, R., & Chen, W. (2012). Solution synthesis, photoluminescence and X-ray luminescence of Eu-doped nanoceria CeO_2:Eu. *Journal of Material Chemistry, 22*, 23461–23467.

Shivram, M., Prashantha, S. C., Nagabhushana, H., Sharma, S. C., Thyagarajan, K., Harikrishna, R., et al. (2014). $CaTiO_3$:Eu^{3+} red nanophosphor: low temperature synthesis and photoluminescence properties. *Spectrochimica Acta Part A: Molecular and Biomolecular Spectroscopy, 120*, 395–400.

Sterrer, M., Fischbach, E., Risse, T., & Freund, H. J. (2005). Geometric characterisation of a singly charged oxygen

vacancy on a single crystalline MgO film by EPR spectroscopy. *Physical Review Letters, 94*, 186101.

Sunitha, D. V., Manjunatha, C., Shilpa, C. J., Nagabhushana, H., Sharma, S. C., Nagabhushana, B. M., et al. (2012). $CdSiO_3:Pr^{3+}$ nanophosphor: synthesis, characterization and thermoluminescence studies. *Spectrochimica Acta Part A: Molecular and Biomolecular Spectroscopy, 99*, 279–287.

Tamboli, S. H., Patil, R. B., Kamat, S. V., Puri, V., & Puri, R. K. (2009). Modification of optical properties of MgO thin films by vapour chopping. *Journal of Alloys and Compounds, 477*, 855–859.

Tauc, J. (1970). In F. Abeles (Ed.), *Optical properties of solids*. Amsterdam: North-Holland.

Tauc, J., Grigorovici, R., & Vancu, A. (1966). Optical properties and electronic structure of amorphous Germanium optical. *Physica Status Solidi (b), 15*, 627–638.

Telex Peter, A., & Waldron, J. R. (1955). Reflectance of magnesium oxide. *Journal of Optical Society of America, 45*, 19.

Van Uitert, L. G. (1967). Characterization of energy transfer interactions between rare earth ions. *Journal of Electro Chemical Society, 114*, 1048–1053.

Venkata Reddy, Ch., Rama Krishna, C., Raghavendra Rao, T., Udayachandran Thampy, U. S., Reddy, Y. P., Rao, P. S., et al. (2012). Synthesis and spectral characterizations of Fe^{3+} doped β-BaB_2O_4 nano crystallite powder. *Journal of Molecular Structure, 1012*, 17–21.

Viagin, O., Masalov, A., Ganina, I., & Malyukin, Y. (2009). Mechanism of energy transfer in Sr2CeO4:Eu3+ phosphor. *Optical Materials, 31*, 1808–1810.

Wang, D., Chen, Z. Q., Li, C. Y., Li, X. F., Cao, C. Y., & Tang, Z. (2012). Correlation between ferromagnetism and defects in MgO nano crystals studied by positron annihilation. *Physica B: Condensed Matter, 407*, 2665–2669.

Wang, Z., Li, P., Yang, Z., & Guo, Q. (2012). A novel red phosphor $BaZn_2(PO_4)_2:Sm^{3+}$, R^+ (R = Li, Na, K). *Journal of Luminesence, 132*, 1944–1948.

Williamson, G. K., & Hall, W. H. (1953). X-ray line broadening from filed aluminium and wolfram. *Acta Metallurgica, 1*, 22–31.

Wyckoff, R. W. G. (1964). *Crystal structures* (pp. 4–5). New York: Interscience.

Yanagida, T., Nagashima, K., Tanaka, H., & Kawai, T. (2008). Easy and effective synthesis of micrometer-sized rectangular MgO sheets with very high catalytic activity. *Journal of Physics, 104*, 016101–016103.

Yang, F., Yang, Z., Yu, Q., Liu, Y., Li, X., & Lu, F. (2013). Sm^{3+} doped $Ba_3Bi(PO_4)_3$ orange reddish emitting phosphor. *Spectrochimica Acta Part A: Molecular and Biomolecular Spectroscopy, 105*, 626–631.

Yang, M., You, H., Liang, Y., Xu, J., Lu, F., Dai, L., et al. (2014). Morphology controllable and highly luminescent monoclinic $LaPO_4:Eu^{3+}$ Microspheres. *Journal of Alloys and Compounds, 582*, 603–608.

Yang, S. Y., & Kim, S. G. (2004). Characterization of silver and silver/nickel composite particles prepared by spray pyrolysis. *Powder Technology, 146*, 185–192.

Yang, K. C., & Shen, P. (2005). On the precipitation of coherent spinel nanoparticles in Ti-doped MgO. *Journal of Solid State Chemistry, 178*, 661–670.

Zou, B., & Volkov, V. (2000). Surface modification on time-resolved fluorescences of Fe2O3 nanocrystals. *Journal of Physics and Chemistry of Solids, 61*, 757–764.